Time-resolved terahertz spectroscopy for probing the effects of low-temperature annealing on $CsPbBr_3$ evaporated thin-films

Lorenzo Gatto[1,2], Antonella Treglia[1,3], Gabriele Crippa[1,2], Michele Devetta[2], Giulia Folpini[3], Annamaria Petrozza[3], Salvatore Stagira[1,2], Caterina Vozzi[2], Eugenio Cinquanta[2]

[1]Dipartimento di Fisica, Politecnico di Milano, 20133, Milano, Italy
[2]Istituto di Fotonica e Nanotecnologie, Consiglio Nazionale delle Ricerche, 20133, Milano, Italy
[3]Center for NanoScience and Technology, Istituto Italiano di Tecnologia, 20133 Milano, Italy

Abstract: The fine-tuning of the growth conditions and post-deposition treatments is of fundamental importance to improve the efficiency of photovoltaic devices based on all-inorganic metal halide perovskites like $CsPbBr_3$. In this work, we used time-resolved terahertz spectroscopy (TRTS) in combination with optical characterization techniques, x-ray diffraction (XRD), and scanning electron microscopy (SEM), to probe the different properties induced by a low-temperature (180 °C) annealing treatment on evaporated $CsPbBr_3$ thin-films. We observed a faster build-up and relaxation dynamics in the annealed sample, accompanied by a remarkable decrease of the photoluminescence (PL) intensity and minor changes in the photoconductivity and XRD measurements as compared to the as-deposited sample. We estimated for both the samples a mobility of $\mu = (1.7 \pm 0.5) \cdot 10^2$ $cm^2\ V^{-1}\ s^{-1}$. Our results suggest that the lattice reorganization induced by low-temperature annealing of evaporated $CsPbBr_3$ could lead to a different charge carrier-phonon coupling and to an increased contribution of non-radiative recombination channels. We found that TRTS can be effectively used to follow the changes induced by post-deposition thermal annealing of $CsPbBr_3$.

Introduction

The advances in the knowledge of metal-halide perovskites demand increasing attention for fabrication techniques, towards the development of competitive industrial applications and manufacturing strategies. The all-inorganic cesium lead bromide ($CsPbBr_3$) stands out in the class of lead-halide perovskites, because of its high stability in a humid environment and promising optoelectronic properties [1]. However, the power conversion efficiency (PCE) of $CsPbBr_3$ solar cells [2] [3] [4] [5] [6] is still far from the record values reached by less stable cells, based on hybrid organic-inorganic [7] or mixed-halide perovskites [8] [9] [10]. The fine control of the thin-film morphology and the crystal lattice defects is extremely important to increase the efficiency of $CsPbBr_3$-based photovoltaics devices and boost further applications.

Several fabrication techniques have been explored to obtain polycrystalline and single-crystal samples of $CsPbBr_3$ [1] [11]. Vapor-based methods can be easily integrated into the established planar processes for the manufacturing of semiconductor technologies. Furthermore, they have proven to give a good film morphology, thickness control, and high reproducibility [1] [12]. Thermal annealing is in this case a critical step to control the physical properties of the deposited material and ultimately the performance of the device.

Time-resolved terahertz spectroscopy (TRTS) has been employed in recent works to estimate the high mobility and diffusion length in colloidal $CsPbBr_3$ nanocrystals (NCs) [13], the optoelectronic and vibrational properties of $CsPbBr_3$ NCs films [14], and low-energy excitations in several inorganic and hybrid perovskites [15] [16] [17]. TRTS has also been used to point out the polaronic nature of the photoinduced charge carriers in lead-halide perovskites and to quantify their formation time [18] [19].

In this work, we used TRTS to study the photoinduced charge-carrier ultrafast dynamics in evaporated samples of $CsPbBr_3$ with different post-deposition treatments. We report on the faster build-up and recombination dynamics, observed on an annealed $CsPbBr_3$ sample, accompanied by minor changes in the THz photoconductivity and a remarkable decrease of the photoluminescence intensity as compared to the as-deposited sample.

Our observations highlight how a fine-tuning of the annealing parameters is needed to obtain the desired improvement of the material quality and the use of TRTS contributes to the outlining of multiple strategies to benchmark different fabrication protocols of $CsPbBr_3$ thin-films.

Methods

Sample synthesis and preparation

Lead(II) bromide ($PbBr_2$, ≥98%) was purchased from Tokyo Chemical Industry (TCI) and cesium bromide (CsBr,99.999%) was purchased from Alfa Aesar. Fused silica substrates were cleaned in acetone and isopropyl alcohol (IPA) for 15 min by sonication. The cleaned substrates were treated with oxygen plasma for 10 min before any further deposition. Perovskite thin-films were deposited by vacuum thermal evaporation (Moorfield) in a chamber installed in a nitrogen-filled glovebox (O_2 and H_2O < 1 ppm) so that samples and source materials can be loaded and unloaded under inert conditions. The precursors were co-evaporated from separate sources at a pressure of $\sim 5\times10^{-7}$ mbar. Initially, the sources were heated to reach the evaporation rate set-point (0.25 Å/s), detected using dedicated quartz crystal microbalances, one for each source. The evaporation temperature was 260 °C and 400 °C for $PbBr_2$ and CsBr, respectively. After a stabilization period of ∼5 minutes, the substrate shutter was opened to allow material deposition onto the substrates for ∼1.5 hours. To maximize the uniformity of the deposition, the sample holder was rotated during the deposition. After deposition, the samples were either tested directly, herein referred to as "as-deposited" or annealed in a nitrogen-filled glovebox at 180 °C for 30 minutes.

Characterization

Microstructure: XRD patterns were recorded with a Bruker D8 Advance diffractometer with Bragg–Brentano geometry equipped with a Cu Kα1 (λ = 1.544060 Å) anode, operating at 40 kV and 40 mA. All the diffraction patterns were collected at room temperature, with a step size of 0.05° in symmetric scan reflection mode and an integration time of 1 s per point.

Thickness: Perovskite film thicknesses were measured using a Veeco Dektak 150 surface profilometer.

Microscopy: SEM images were obtained using a MIRA3 TESCAN microscope with an accelerating voltage of 5 kV.

UV-vis absorption: steady-state absorption spectra were measured using a UV/VIS/NIR spectrophotometer Lambda 1050 PerkinElmer, in the wavelength range 250-700 nm, with a step size of 1 nm.

Steady State Photoluminescence: PL spectra were measured following excitation by a 450 nm continuous wave laser (Oxxius) with a power density of 100 mW/cm^2. PL was collected in reflection mode and focused into a fiber coupled to a spectrometer (Ocean Optics Maya Pro 2000).

Ultrafast THz spectroscopy

Our terahertz (THz) spectroscopy setup is driven by a Ti:Sapphire amplified laser system, delivering 35-fs pulses with a repetition rate of 1 kHz centered at $\lambda \approx$ 790 nm. A pulse energy of approximately 1 mJ is delivered to the THz setup and split into three lines devoted to THz generation, THz detection (gate), and sample photoexcitation (pump). For this experiment, THz pulses are generated by optical rectification in a ZnTe crystal, 1 mm-thick and <110>-oriented. This gives a probe bandwidth between 0.4 THz and 2.1 THz. The pump pulse can be obtained either by second harmonic generation or by an optical parametric amplifier tunable in the visible range. The pump pulse is focused on the sample with a spot size of ∼2.5 mm. The THz pulse is directed to the sample by off-axis parabolic mirrors, obtaining a probe spot-size at the sample of ∼1 mm. The transmitted THz pulse is then reconstructed in the time domain by electro-optic sampling (EOS), exploiting the interaction of the THz electric field with the gate pulse in a ZnTe detector crystal, with the same characteristics of the emitter. The sample is at room temperature and the THz pulses propagate in a chamber purged by dry-nitrogen, to avoid THz absorption by water vapor.

In the pump-probe measurements, the generation and pump beam are simultaneously modulated by an optical chopper at two different frequencies. This approach, described in reference [20], allows to simultaneously demodulate with a lock-in amplifier both the pump-probe differential signal $\Delta E = E_{on} - E_{off}$ and the pump-off signal E_{off}. For this work we used pump pulses either at $\lambda \approx$ 500 nm, nearly resonant with the band-gap of $CsPbBr_3$, or at $\lambda \approx$ 400 nm to photoinject charges in the conduction band.

We characterize the response of the samples in the probe spectral range by THz time-domain spectroscopy (THz-TDS). We measure the electric field of the transmitted probe pulse through the sample and the reference substrate. The ratio of the Fourier transforms of the two wave-forms gives a complex transmission function $T(\omega)$. This can be used to compute the static conductivity through an approximated formula, commonly adopted in the THz-TDS analysis of thin-films [21]:

$$\sigma(\omega) = \frac{n_1 + n_2}{dZ_0}\left(\frac{1}{T(\omega)} - 1\right) \quad (1)$$

where n_1 and n_2 are the refractive indices of the media surrounding the sample, *d* is the thickness of the thin film and Z_0 is the impedance of free space. In our case n_1 and n_2 are the refractive indices of dry-nitrogen and the fused silica substrate, respectively.

We study the transient response with two different acquisition modes. The first one is fixing the EOS delay at the THz pulse peak and measuring the relative change of the signal as a function of the pump-probe delay τ (''1D scan'' as in reference [22]). This approach gives access to frequency integrated pump-probe dynamics [23]. The second mode consists in scanning both the EOS and the pump delay lines, acquiring the relative change of the full THz wave-forms (''2D scan'' as in reference [22]). As explained above, we measure simultaneously the differential signal ΔE and the pump-off signal E_{off}. In the case of the 2D scan these are Fourier transformed and used to compute the complex transmission function $T^*(\omega,\tau) = \frac{\Delta E(\omega,\tau)}{E_{off}(\omega)} + 1$. This can be used to retrieve the complex response function of the photoexcited material in the frequency domain. This result is usually expressed in terms of photoconductivity $\Delta\sigma(\omega,\tau) = -\mathrm{i}\omega\varepsilon_0\Delta\varepsilon(\omega,\tau)$, where $\Delta\varepsilon$ is the pump-induced change of the material dielectric function.

The transient THz response of intrinsic or low-doped semiconductor thin-films is commonly evaluated by an approximated analytical formula [21] [24]. This directly relates the photoconductivity to the complex transmission function T^*:

$$\Delta\sigma(\omega,\tau) = \frac{n_1 + n_2}{d_f^* Z_0}\left(\frac{1}{T^*(\omega,\tau)} - 1\right) \quad (2)$$

where n_1 and n_2 are the refractive indices of the media surrounding the photoexcited layer of the film, d_f^* is the thickness of the photoexcited layer and Z_0 is the impedance of free space. In our case n_1 and n_2 are the refractive indices of dry-nitrogen and the non-photoexcited part of the material, respectively. We used a photoexcited film thickness of 100 nm, estimated from the optical absorption coefficient at the pump wavelength. The validity of the thin-film approximation for a photoexcited layer with complex refractive index $n_f^* + i\kappa_f^*$ and thickness d_f^*, is quantified by the conditions $n_f^*\frac{\omega}{c}d_f^* \ll 1$ and $\kappa_f^*\frac{\omega}{c}d_f^* \ll 1$ [24]. We cross-checked the fulfillment of these conditions by computing $n_f^* + i\kappa_f^*$ from $\Delta\sigma$ and the static dielectric function measured by THz-TDS. If $\frac{\Delta E(\omega,\tau)}{E_{off}(\omega)} \ll 1$ the equation (2) can be further simplified as:

$$\Delta\sigma(\omega,\tau) = -\frac{n_1 + n_2}{d_f^* Z_0}\cdot\frac{\Delta E(\omega,\tau)}{E_{off}(\omega)} \quad (3)$$

In the following, we are going to use equation (2), since it gives a better estimate of the photoconductivity spectra compared to equation (3) [21] [25]. Equation (3) is nevertheless useful to understand the common interpretation of the 1D scans signal as a measurement of the sample photoconductivity. More specifically, the relative change of the THz pulse peak and zero-crossing are often interpreted as a measurement of the frequency-averaged real and imaginary parts of $\Delta\sigma(\omega,t)$, respectively. This is obviously true when $\Delta\sigma$ in equation (3) is approximately real and frequency-independent (Drude model with $\omega\tau \ll 1$), but for a more general behavior the relation has to be carefully evaluated [23]. We checked that the pump-probe dynamics $-\Delta E(t_{peak},\tau)/E_{off}(t_{peak})$ obtained from the measured 2D scans, follows the same trend of the frequency-integrated real part of $\Delta\sigma(\omega,\tau)$ obtained by equation (3) (see supplementary information). The comparison indicates that the pump-probe dynamics is in good approximation proportional to the frequency averaged real photoconductivity. Consequently, the estimated recombination rate constants can be interpreted as those of the polaronic charge carriers.

The build-up of the pump-probe signal can require a formation time larger than the instrumental response function (IRF), due to the generation of a population of hot-carriers. The carrier cooling and the

subsequent formation of polarons is considered to be the leading mechanism in the build-up of the transient THz response in $CsPbBr_3$ and similar lead-halide perovskites [18] [19]. Following this idea, we fitted the build-up dynamics using the simplified model proposed in reference [19]. This is based on the solution of a system of linear rate equations, which represent a three-level system, where hot-carriers are converted progressively into cold-carriers and eventually into polarons. The solution of the rate equations system is:

$$n(t) = n\left[\frac{1}{\tau_{cool} - \tau_{pol}}\left(\tau_{pol}e^{-\frac{t}{\tau_{pol}}} - \tau_{cool}e^{-\frac{t}{\tau_{cool}}}\right) + 1\right] \qquad (4)$$

To fit the data, we used equation (4) convolved with a gaussian function with a full-width at half-maximum (FWHM) of 100 fs to take into account the effect of the IRF. This is estimated considering the convolution of the pump pulse with the gate pulse, used to sample the THz waveform peak.

The relaxation dynamics can be fitted using the numerical solution of the following rate equation:

$$\frac{dn}{dt} = -k_1 n - k_2 n^2 - k_3 n^3 \qquad (5)$$

where trap-assisted, band-to-band, and Auger recombination channels are considered [15] [16]. Since the pump-probe signal can be considered proportional to the polaron density, the parameters extracted by the fit of the dimensionless signal can be converted into the recombination rate k_1 and the apparent rates $k_2\phi$ and $k_3\phi^2$, where ϕ is referred to as photon-to-carrier branching ratio (see supplementary information and reference [16] for more details).

Results and Discussion

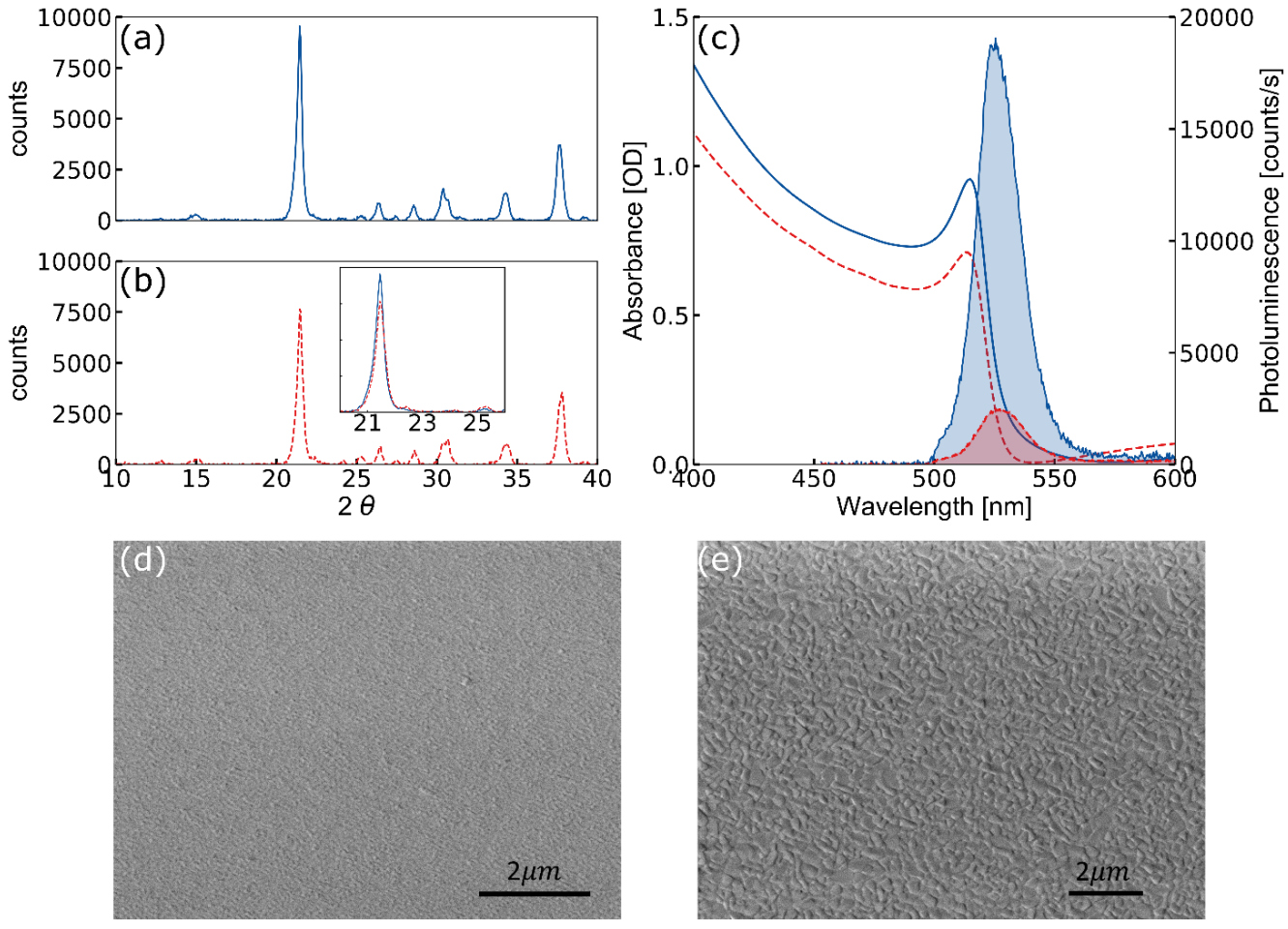

Figure 1 (a)-(b) X-ray diffraction (XRD) measurements of the as-deposited and annealed samples. The inset in (b) highlights the small reduction of the peak at 21.45° in the annealed sample. (c) Optical absorption and photoluminescence (PL) of the as-deposited (blue solid line) and annealed (red dashed line) samples. (d)-(e) scanning electron microscopy (SEM) images of the as-deposited and annealed samples.

In Figure 1 we report XRD measurements (a)-(b) and SEM images (d)-(e) of the two samples. The SEM images confirm the increased grain size, expected after the annealing process. We estimate a grain size of (63±3) nm and (302±13) nm respectively for as-deposited and annealed samples (see supplementary information, figure S1). In Figure 1(c) we plot the optical absorbance and the PL spectra. In the visible range, we can see a slight decrease in the absorbance after the annealing and a remarkable lowering of the PL intensity. The XRD measurements on the two samples (Figure 1(a)-(b)) confirm that the material presents a good crystallinity and forms a prevalent $CsPbBr_3$ orthorhombic phase with both the fabrication protocols. However, the small changes of relative intensity and shape of the XRD peaks (see the peak at $2\theta \approx 21.45°$ in Figure 1 (a)-(b)) may be also related to a reduced $CsPbBr_3$ volume fraction in favor of different phases [26]. It is possible that the morphological reorganization, induced by the low-temperature annealing, is responsible for the formation of point and/or extended defects.

For example, the thermodynamically stable $CsPb_2Br_5$ phase has a formation enthalpy similar to that of $CsPbBr_3$ [27] and, as pointed out in reference [26], it can add deep recombination centers at the $CsPbBr_3$/$CsPb_2Br_5$ interface. These can provide non-radiative recombination channels, which quench the photoluminescence intensity. We stress here that a different outcome could be obtained annealing at higher temperatures [28], since a different amount of thermal energy is delivered to the crystal lattice, and different regions of the perovskite phase diagram are explored [11].

On the other hand, since the annealing temperature is higher than the orthorhombic-to-tetragonal phase transition temperature (88 °C [29]), the stress induced in the lattice can lead to the formation of vacancies and substitutional defects [11]. These can also act as deep trap states and contribute to non-radiative recombination channels.

Figure 2 shows the static conductivity retrieved as described in the methods section. The as-deposited sample presents an absorption feature superimposed over a broader absorption band at ~2 THz, compatible with the presence of an IR-active phonons. After the gentle annealing, the static THz response reveals a broad feature at ~1.7 THz. Moreover, the annealed sample is characterized by a lower absorption of our THz probe, as indicated by the lower real part of the conductivity. We conclude that a lattice reorganization induced by the annealing is responsible for the different IR activity of the sample.

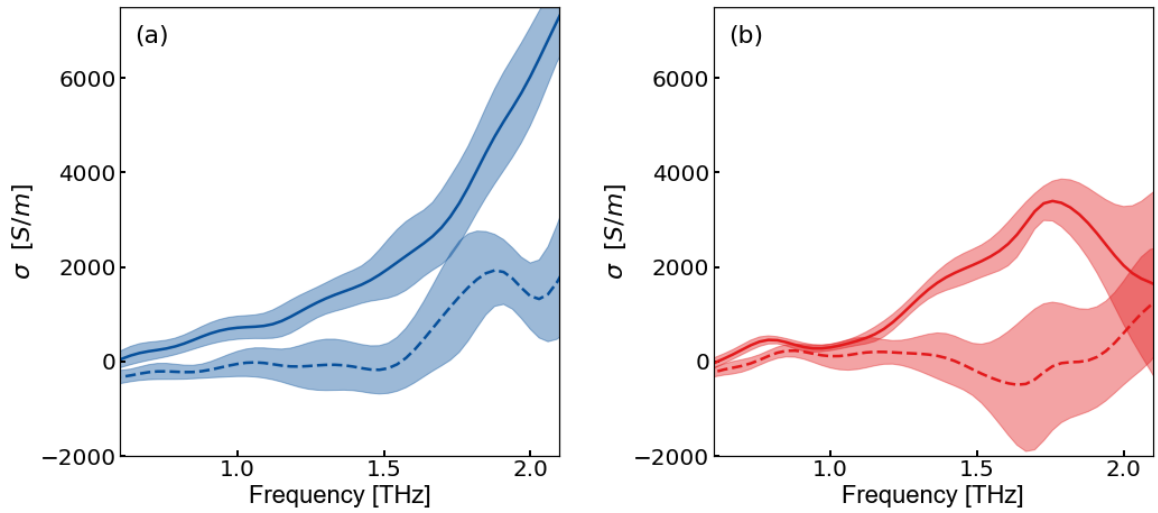

Figure 2 Real (solid line) and imaginary (dashed line) static conductivity of the as-deposited (a) and annealed (b) samples.

We now focus on the relative change of the transmitted THz pulse peak after the photoexcitation of the sample with a 400 nm pump pulse. The first 200 picoseconds of the relaxation dynamics of the as-

deposited and annealed samples at three different pump fluences are shown in Figure 3(a) and (b) respectively. We report in the insets the build-up and the relaxation up to a pump-probe delay of 20 ps.
The relaxation dynamics of the annealed sample emerged to be faster compared to the as-deposited one, especially at the two highest pump fluences, where the role of many-body recombination processes becomes important. A larger grain size is usually expected to give a slower dynamics and a longer diffusion length [28], because of the lower concentration of grain boundaries. We consider that the formation of point and/or extended defects induced by the annealing process can contribute to recombination channels, dominating over the opposite effect of the increased grain size.

A global fitting of the dynamics is performed using equation (5) (see supplementary information). The monomolecular (trap-assisted) recombination happens on a time-scale much longer than the investigated window [13] [17] [30], therefore it does not significantly affect our measurements. Consequently, following the approach or reference [17], we fixed a value of $k_1 = 10^9\ s^{-1}$ (compare with reference [30] for evaporated $CsPbBr_3$) to obtain an estimate of the apparent rate constants $k_2\phi$ and $k_3\phi^2$. The results corresponding to the fit reported in **Figure 3** are $k_2\phi = 2 \cdot 10^{-10}\ cm^3 s^{-1}$, $k_3\phi^2 = 6 \cdot 10^{-28}\ cm^6 s^{-1}$ for the as deposited sample, and $k_2\phi = 1 \cdot 10^{-9}\ cm^3 s^{-1}$, $k_3\phi^2 = 2 \cdot 10^{-27}\ cm^6 s^{-1}$ for the annealed sample.

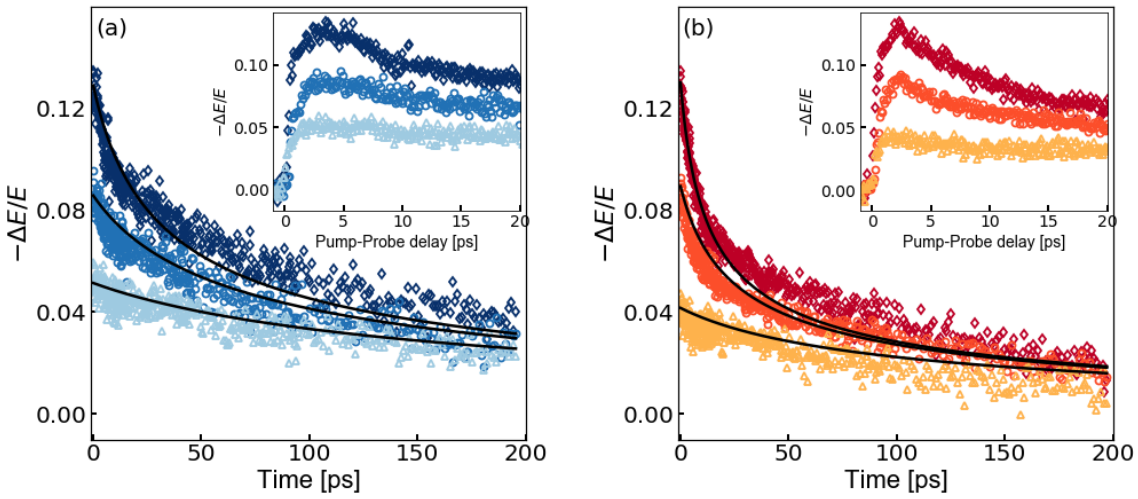

Figure 3 400 nm pump-THz probe dynamics of the (a) as-deposited and (b) annealed samples. Darker colors correspond to higher pump fluence: (a) $44.8\ \mu J/cm^2$ (dark blue diamonds) – $26.5\ \mu J/cm^2$ (blue circles) – $13.9\ \mu J/cm^2$ (light blue triangles). (b) $46.9\ \mu J/cm^2$ (red diamonds) - $23.4\ \mu J/cm^2$ (orange circles) - $15.6\ \mu J/cm^2$ (yellow triangles). The black solid lines represent the result of a global fit based on a rate equations model. The insets show the build-up and the relaxation up to 20 ps.

The faster relaxation observed for the annealed sample corresponds to larger apparent rate constants extracted by the fit. The rate constants present a reasonable agreement with those found in reference [30] for evaporated thin-films of $CsPbBr_3$ and with the results of reference [17] for spin-coated samples of $FAPbBr_3$.

To reveal the influence of the annealing process on the polaron formation, we exploited pump pulses resonant with the band-gap. As reported in Figure 1(c), the 500 nm pump can photoinject free carriers right above the conduction band edge, while the 400 nm pump generates hot-carriers with larger excess energy.

The first picoseconds of the normalized dynamics of the as-deposited and annealed samples acquired with the 400 nm and 500 nm are shown in Figure 4. For the as-deposited sample (Figure 4 (a)) the build-up dynamics obtained with the 500 nm pump is faster than the one obtained with 400 nm, reflecting the lower excess energy of the photogenerated hot-carriers [19].

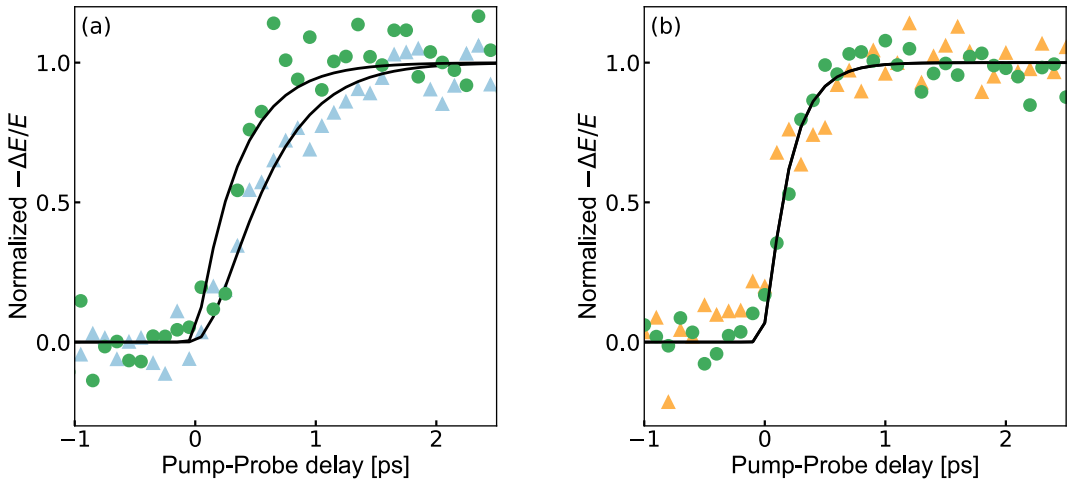

Figure 4 Signal build-up dynamics for the (a) as-deposited and (b) annealed sample with a 500 nm pump (pump fluence: $14.7\ \mu J/cm^2$ green circles) and a 400 nm pump (pump fluence: $13.9\ \mu J/cm^2$ (a) light blue triangles and $15.6\ \mu J/cm^2$ (b) yellow triangles). The black solid lines represent the fits based on a rate equations model (see equation (4)).

Thanks to the fitting procedure based on equation (4), we estimated a cooling time τ_{cool} of 0.27 ps at 400 nm with a polaron formation time τ_{pol} of 0.35 ps. At 500 nm the build-up can be fitted by the same τ_{pol}, but with a τ_{cool} shorter than the IRF (tens of fs). In contrast, for the annealed sample (Figure 4(b)), the rise time at 400 nm is faster compared to the one of the as-deposited sample and it results to be excess energy independent. From the fit at both the excitation wavelengths, we obtained indeed a polaron formation time around 0.20 ps and a cooling time of the hot carriers τ_{cool} shorter than the IRF (tens of fs).

Further insight into the transient THz response is given by the photoconductivity spectra. In Figure 5 we report the complex photoconductivity (equation (2)) of the as-deposited (a-b-c) and annealed (d-e-f) samples at a fixed pump-probe delay, corresponding 3 ps and 2 ps respectively. The pump-probe delay is chosen so that it matches that of the maximum signal in the 1D scans (insets of Figure 3).

The scattering at the grain boundaries in polycrystalline samples can lead to a photoconductivity following a Drude-Smith response [31] [32], rather than the simple Drude model. Therefore, we analyzed the photoconductivity spectra using the Drude-Smith model (see Figure 5), to obtain an estimate of the carrier mobility (as explained in reference [13] for $CsPbBr_3$ nanocrystals). We used an effective mass for the polaronic carriers of $m^* = 3.5 \cdot (0.21 \cdot m_e)$ [18]. We obtained for both samples a value of $\mu = (1.7 \pm 0.5) \cdot 10^2$ cm^2 V^{-1} s^{-1}, where the error is estimated from the uncertainties on the scattering rates, extracted from the Drude-Smith fit. This indicates that the adopted low-temperature annealing is not leading to an increased mobility. Interestingly, the extracted value is slightly larger than values previously reported in the literature [18] [33]. This suggests a possible advantage of the physical vapor deposition approach, compared to the different growth conditions studied in the cited works. This needs to be confirmed by an independent mobility characterization, such as a Hall-effect measurement. Following reference [34], we used a carrier density of n = 10^{14} cm^{-3}, representative of low-level solar illumination, with a total recombination rate $R_{tot} = n^2 k_3 + nk_2 + k_1 \approx k_1 = 10^9$ s^{-1} [30], to estimate the diffusion length. The result is $L_D = \sqrt{\frac{D}{R_{tot}(n)}} \approx 0.7\ \mu$m, where $D = \frac{\mu k_B T}{e}$ is the diffusion coefficient containing the mobility extracted from the fit of the photoconductivity spectra.

We can observe that peaks in the real part correspond to inflection points in the imaginary part. As the photoconductivity is related to the complex dielectric function change by the relation $\Delta\sigma = -i\omega\varepsilon_0\Delta\varepsilon$, the peaks in the real part of $\Delta\sigma$ correspond to peaks in the imaginary part of $\Delta\varepsilon$. The photoconductivity can be related to a pump-induced transient absorption of THz radiation, by quasi-free carriers or more generally by collective vibrational modes of the system modified by the action of the pump pulse.

In this case, the transient response of the system is characterized by several absorption features. It is known that the THz response of $CsPbBr_3$ and similar lead-halide perovskites can be explained in terms of large

polarons [35] [18]. These emerge due to the coupling between the photogenerated charge carriers and the vibrational modes of the soft ionic lattice. This coupling appears as absorption features in the photoconductivity spectra.

The differences observed according to the pump fluence could in fact arise from a dissimilar carrier-phonon coupling in different regions of the samples. Therefore, these changes could be interestingly interpreted as a qualitative evaluation of the sample inhomogeneity. Nevertheless, the frequency averaged dynamics of the two samples present a clear difference at all the pump fluences and the Drude-Smith fitting of the photoconductivity is describing only the overall frequency response. Consequently, the quantitative results presented in the article are not affected by these changes.

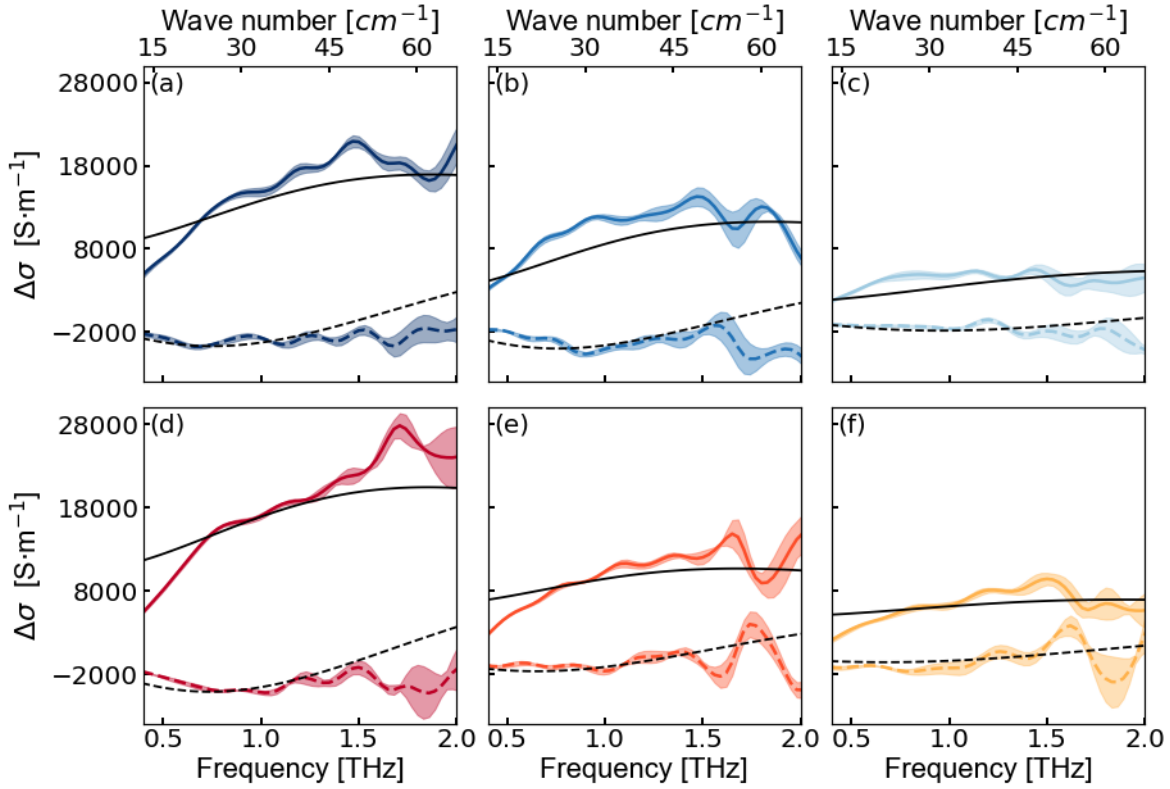

Figure 5 400 nm pump-THz probe measurements. Real (solid line) and imaginary (dashed line) part of the photoconductivity of the (a-b-c) as-deposited and (d-e-f) annealed sample, retrieved at a pump-probe delay of 3 ps and 2 ps respectively. The 400 nm pump fluence are (a) $44.8\ \mu J/cm^2$, (b) $26.5\ \mu J/cm^2$, (c) $13.9\ \mu J/cm^2$, (d) $46.9\ \mu J/cm^2$, (e) $23.4\ \mu J/cm^2$, (f) $15.6\ \mu J/cm^2$. The black solid (dashed) lines represent the real (imaginary) part of the Drude-Smith conductivity.

In Figure 6 we can follow the evolution of the real part of the photoconductivity spectra as the pump-probe delay increases for the as-deposited (a)-(b)-(c) and annealed (d)-(e)-(f) samples.

The frequency behavior does not present remarkable differences between the two samples, confirming the polaronic nature of response with both the fabrication processes. We can nevertheless point out some minor changes in the shape and relative intensity of the peaks. Furthermore, the time evolution of the real photoconductivity reflects the dynamics observed in Figure 3. This suggests that the material modifications due to the adopted annealing conditions lead to more efficient cooling of the hot carriers with a consequent faster formation time of the polarons and to higher recombination rates in the first hundreds of picoseconds after the photoexcitation.

The quenching of the PL emission and the different behavior probed by frequency-averaged and frequency-resolved THz spectroscopy in the first picoseconds after the photoexcitation can be ascribed to the different lattice environment created by the annealing process, as previously discussed (see Figure 1 and related discussion). This is also supported by the small changes observed in the photoconductivity spectra, which reflects the charge carrier-phonon coupling. Moreover, different vibrational modes introduced by the

point defects could imply a different coupling as well with the photoexcited charge carriers and appear as a different transient response in the photoconductivity spectra and as a different optical pump-THz probe dynamics.

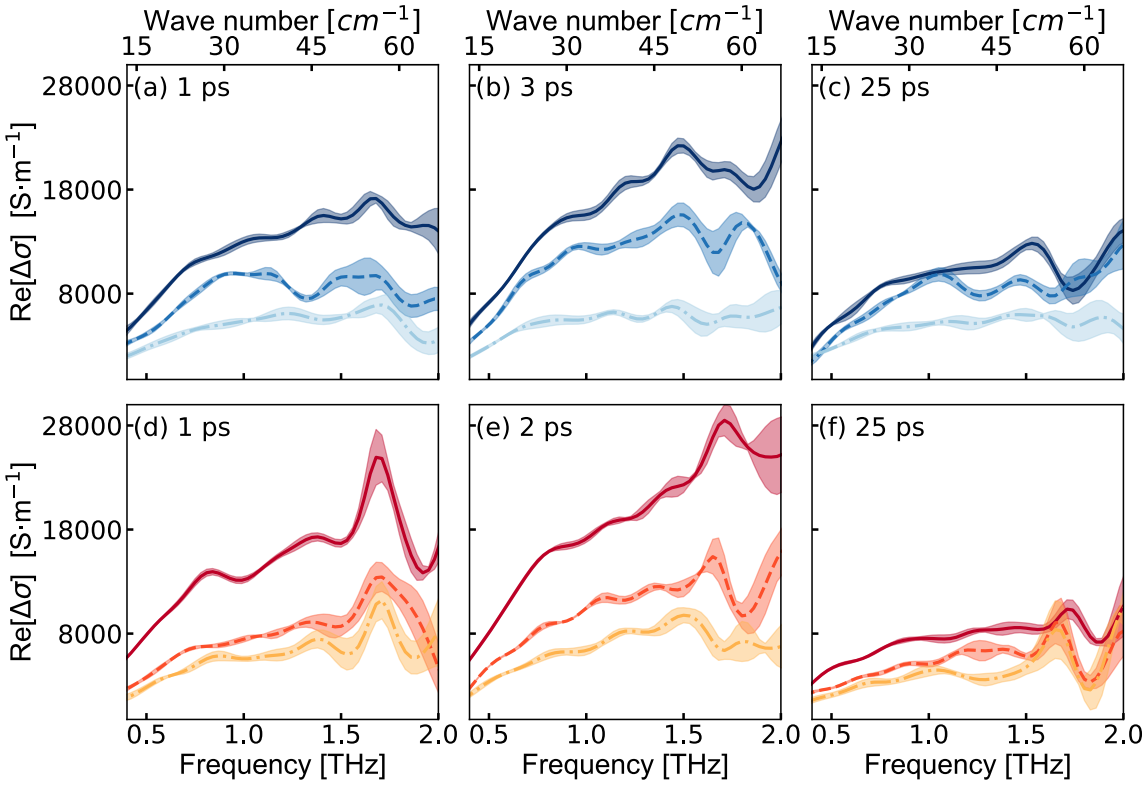

Figure 6 400 nm pump-THz probe measurements. Real part of the photoconductivity retrieved for the (a-b-c) as-deposited and (d-e-f) annealed sample at different pump-probe delays and pump fluences. (a-b-c) correspond respectively to delays of 1-3-25 ps, while (d-e-f) to 1-2-25 ps. Darker colors correspond to higher pump fluence: (a-b-c) $44.8\ \mu J/cm^2$ (dark blue solid line) – $26.5\ \mu J/cm^2$ (blue dashed line) – $13.9\ \mu J/cm^2$ (light blue dot-dashed line). (d-e-f) $46.9\ \mu J/cm^2$ (red solid line) - $23.4\ \mu J/cm^2$ (orange dashed line) - $15.6\ \mu J/cm^2$ (yellow dot-dashed line).

Conclusion

In conclusion, we studied the effects of a low-temperature annealing process on $CsPbBr_3$ samples, deposited by vacuum thermal evaporation. We employed THz spectroscopy to highlight the different behavior of the annealed material compared to the as-deposited one. We completed our observations with optical absorption, PL, XRD, and SEM measurements. By 400 nm pump-THz probe measurements we observed faster build-up and relaxation dynamics in the annealed sample, accompanied by a remarkable decrease of the PL intensity. Small changes are observed in the THz photoconductivity and XRD measurements, indicating only a partial reorganization of the material. This is associated with a modification of the morphology of the thin-film, presenting an increased grain size after the annealing process. We estimated for both the samples a mobility of $\mu = (1.7 \pm 0.5) \cdot 10^2$ cm^2 V^{-1} s^{-1}.

Further investigations are needed to better understand the effects of different annealing conditions on $CsPbBr_3$ evaporated films and to clarify how TRTS can be leveraged to monitor the effects of different fabrication protocols. Our outcomes indicate that TRTS can be sensitive to the modifications induced by post-deposition thermal annealing of $CsPbBr_3$. Furthermore, they suggest that low-temperature annealing of evaporated $CsPbBr_3$ could lead to measurable changes of the charge carrier-phonon coupling and to an increased contribution of non-radiative recombination channels.

Data Availability Statement

The datasets generated during and/or analyzed during the current study are available from the corresponding author on reasonable request.

Acknowledgments

EC, CV, LG, SS acknowledge financial support from MIUR PRIN aSTAR (Grant No. 2017RKWTMY), and from European Union's Horizon 2020 research and innovation program through the MSCA-ITN SMART-X (GA 860553). GF and AP acknowledge the funding from the European Union's Horizon 2020 research and innovation program through the ERC project SOPHY under grant agreement no. 771528.

References

[1] Saad Ullah, Jiaming Wang, Peixin Yang, Linlin Liu, Shi-E. Yang, Tianyu Xia, Haizhong Guo and Yongsheng Chen, "All-inorganic CsPbBr3 perovskite: a promising choice for photovoltaics," *Mater. Adv.,* vol. 2, p. 646, 2021.

[2] Guoqing Tong, Taotao Chen, Huan Li, Longbin Qiu, Zonghao Liu, Yangyang Dang, Wentao Song, Luis K. Ono, Yang Jiang, Yabing Qi, "Phase transition induced recrystallization and low surface potential barrier leading to 10.91%-efficient CsPbBr3 perovskite solar cells," *Nano Energy,* vol. 65, p. 104015, 2019.

[3] Jingwei Zhu, Mixue Tang, Benlin He, Wenyu Zhang, Xueke Li, Zekun Gong, Haiyan Chen, Yanyan Duanc and Qunwei Tang, "Improved charge extraction through interface engineering for 10.12% efficiency and stable CsPbBr3 perovskite solar cells," *J. Mater. Chem. A,* vol. 8, p. 20987, 2020.

[4] Haiwen Yuan, Yuanyuan Zhao, Jialong Duan, Yudi Wang, Xiya Yang and Qunwei Tang , "All-inorganic CsPbBr3 perovskite solar cell with 10.26% efficiency by spectra engineering," *J. Mater. Chem. A,* vol. 6, p. 24324, 2018.

[5] Jie Lei, Fei Gao, Haoxu Wang, Juan Li, Jiexuan Jiang, Xin Wu, Rongrong Gao, Zhou Yang, Shengzhong (Frank) Liu, "Efficient planar CsPbBr3perovskite solar cells by dual-source vacuum evaporation," *Solar Energy Materials and Solar Cells,* vol. 187, pp. 1-8, 2018.

[6] Weijie Chen, Jingwen Zhang, Guiying Xu, Rongming Xue, Yaowen Li, Yinhua Zhou, Jianhui Hou, and Yongfang Li, "A Semitransparent Inorganic Perovskite Film for Overcoming Ultraviolet Light Instability of Organic Solar Cells and Achieving 14.03% Efficiency," *Adv. Mater.,* vol. 30, p. 1800855, 2018.

[7] Jaeki Jeong, Minjin Kim, Jongdeuk Seo, Haizhou Lu, Paramvir Ahlawat, Aditya Mishra, Yingguo Yang, Michael A. Hope, Felix T. Eickemeyer, Maengsuk Kim, Yung Jin Yoon, In Woo Choi, Barbara Primera Darwich, Seung Ju Choi, Yimhyun Jo, Jun Hee Lee, Bright Walk,, "Pseudo-halide anion engineering for α-FAPbI3 perovskite solar cells," *Nature,* vol. 592, p. 381–385, 2021.

[8] Jingjing Tian, Qifan Xue, Qin Yao, Ning Li, Christoph J. Brabec and Hin-Lap Yip, "Inorganic Halide Perovskite Solar Cells: Progress and Challenges," *Adv. Energy Mater.,* vol. 10, p. 2000183, 2020.

[9] Qiufeng Ye,Yang Zhao, Shaiqiang Mu, Fei Ma, Feng Gao, Zema Chu, Zhigang Yin, Pingqi Gao, Xingwang Zhang, Jingbi You, "Cesium Lead Inorganic Solar Cell with Efficiency beyond 18% via Reduced Charge Recombination," *Adv. Materials,* vol. 31, p. 1905143, 2019.

[10] Ze Qing Lin, Hong Wei Qiao, Zi Ren Zhou, Yu Hou, Xiaolong Li, Hua Gui Yang and Shuang Yang, "Water assisted formation of highly oriented CsPbI2Br perovskite films with the solar cell efficiency exceeding 16%," *J. Mater. Chem. A,* vol. 8, p. 17670, 2020.

[11] Jiaoxian Yu, Guangxia Liu, Chengmin Chen, Yan Li, Meirong Xu, Tailin Wang, Gang Zhaoe and Lei Zhang, "Perovskite CsPbBr3 crystals: growth and applications," *J. Mater. Chem. C,* vol. 8, p. 6326, 2020.

[12] Mingzhen Liu, Michael B. Johnston and Henry J. Snaith, "Efficient planar heterojunction perovskite solar cells by vapour deposition," *Nature,* vol. 501, p. 395–398, 2013.

[13] Gurivi Reddy Yettapu, Debnath Talukdar, Sohini Sarkar, Abhishek Swarnkar, Angshuman Nag, Prasenjit Ghosh and Pankaj Mandal, "Terahertz Conductivity within Colloidal CsPbBr3 Perovskite Nanocrystals:

Remarkably High Carrier Mobilities and Large Diffusion Lengths," *Nano Lett.,* vol. 16, p. 4838−4848, 2016.

[14] Silvia G. Motti, Franziska Krieg, Alexandra J. Ramadan, Jay B. Patel, Henry J. Snaith, Maksym V. Kovalenko, Michael B. Johnston, and Laura M. Herz, "CsPbBr3 Nanocrystal Films: Deviations from Bulk Vibrational and Optoelectronic Properties," *Adv. Funct. Mater.,* vol. 30, no. 1909904, 2020.

[15] Daming Zhao and Elbert E. M. Chia, "Free Carrier, Exciton, and Phonon Dynamics in Lead-Halide Perovskites Studied with Ultrafast Terahertz Spectroscopy," *Adv. Optical Mater.,* vol. 8, p. 1900783, 2020.

[16] Christian Wehrenfennig, Giles E. Eperon, Michael B. Johnston, Henry J. Snaith, and Laura M. Herz, "High Charge Carrier Mobilities and Lifetimes in Organolead Trihalide Perovskites," *Advanced Materials,* vol. 26, no. 10, p. 1584–1589, 2014.

[17] Waqaas Rehman , Rebecca L. Milot , Giles E. Eperon , Christian Wehrenfennig , Jessica L. Boland , Henry J. Snaith , Michael B. Johnston , and Laura M. Herz, "Charge-Carrier Dynamics and Mobilities in Formamidinium Lead Mixed-Halide Perovskites," *Advanced Materials,* vol. 27, p. 7938–7944, 2015.

[18] Eugenio Cinquanta, Daniele Meggiolaro, Silvia G. Motti, Marina Gandini, Marcelo J. P. Alcocer, Quinten A. Akkerman, Caterina Vozzi, Liberato Manna, Filippo De Angelis, Annamaria Petrozza and Salvatore Stagira, "Ultrafast THz Probe of Photoinduced Polarons in Lead-Halide Perovskites," *Physical Review Letters,* vol. 122, p. 166601, 2019.

[19] Simon A. Bretschneider, Ivan Ivanov, Hai I. Wang, Kiyoshi Miyata, Xiaoyang Zhu and Mischa Bonn, "Quantifying Polaron Formation and Charge Carrier Cooling in Lead-Iodide Perovskites," *Advanced Materials,* vol. 30, pp. 1707312-1707312, 2018.

[20] Krzysztof Iwaszczuk , David G. Cooke, Masazumi Fujiwara, Hideki Hashimoto and Peter Uhd Jepsen, "Simultaneous reference and differential waveform acquisition in time-resolved terahertz spectroscopy," *Optic Express,* vol. 17, no. 24, pp. 21969-21976, 2009.

[21] Aleksander M. Ulatowski, Laura M. Herz, Michael B. Johnston, "Terahertz Conductivity Analysis for Highly Doped Thin-Film Semiconductors," *J Infrared Milli Terahz Waves,* vol. 41, p. 1431–1449, 2020.

[22] Matthew C. Beard, Gordon M. Turner, and Charles A. Schmuttenmaer, "Transient photoconductivity in GaAs as measured by time-resolved terahertz spectroscopy," *Physical Review B,* vol. 62, no. 23, p. 15764, 2000.

[23] P. D. Cunningham, "Accessing Terahertz Complex Conductivity Dynamics in the Time-Domain," *IEEE Transactions on Terahertz Science and Technology,* vol. 3, no. 4, pp. 494-498, 2013.

[24] Jens Neu, Kevin P. Regan, John R. Swierk and Charles A. Schmuttenmaer, "Applicability of the thin-film approximation in terahertz photoconductivity," *Applied Physics Letters,* vol. 113, p. 231104, 2018.

[25] Chan La-o-vorakiat, Liang Cheng, Teddy Salim, Rudolph A. Marcus, Maria-Elisabeth Michel-Beyerle, Yeng Ming Lam and Elbert E. M. Chia, "Phonon features in terahertz photoconductivity spectra due to data analysis artifact: A case study on organometallic halide perovskites," *Appl. Phys. Lett.,* vol. 110, p. 123901, 2017.

[26] Sebastián Caicedo-Dávila, René Gunder, José A. Márquez, Sergiu Levcenko, Klaus Schwarzburg, Thomas Unold, and Daniel Abou-Ras, "Effects of Postdeposition Annealing on the Luminescence of Mixed-Phase CsPb2Br5/CsPbBr3 Thin Films," *J. Phys. Chem. C,* vol. 124, p. 19514−19521, 2020.

[27] Sebastián Caicedo-Dávila, Hannah Funk, Robert Lovrinčić, Christian Müller, Michael Sendner, Oana Cojocaru-Mirédin, Frederike Lehmann, René Gunder, Alexandra Franz, Sergej Levcenco, Ayala V. Cohen, Leeor Kronik, Benedikt Haas, Christoph T. Koch and , "Spatial Phase Distributions in Solution-Based and Evaporated Cs−Pb−Br Thin Films," *J. Phys. Chemistry C,* vol. 123, p. 17666−17677, 2019.

[28] Ayuki Murata, Tatsuya Nishimura, Hirofumi Shimizu, Yuta Shiratori, Takuya Kato, Ryousuke Ishikawa and Shinsuke Miyajima, "Effect of high-temperature post-deposition annealing on cesium lead bromide thin films deposited by vacuum evaporation," *AIP Advances,* vol. 10, p. 045031, 2020.

[29] Shunsuke Hirotsu, Jimpei Harada, Masashi Iizumi, and Kazuo Gesi, "Structural Phase Transitions in CsPbBr3," *J. Phys. Soc. Jpn.,* vol. 37, pp. 1393-1398, 1974.

[30] Peipei Du, Jinghui Li, Liang Wang, Liang Sun, Xi Wang, Xiang Xu, Longbo Yang, Jincong Pang, Wenxi Liang, Jiajun Luo, Ying Ma and Jiang Tang, "Efficient and large-area all vacuum-deposited perovskite light-emitting diodes via spatial confinement," *Nature Communications,* vol. 12, p. 4751, 2021.

[31] Ronald Ulbricht, Euan Hendry, Jie Shan, Tony F. Heinz, and Mischa Bonn, "Carrier dynamics in semiconductors studied with time-resolved terahertz spectroscopy," *Rev. Mod. Phys.,* vol. 83, p. 543, 2011.

[32] Gordon M. Turner, Matthew C. Beard, and Charles A. Schmuttenmaer, "Carrier Localization and Cooling in Dye-Sensitized Nanocrystalline Titanium Dioxide," *J. Phys. Chem. B,* vol. 106, pp. 11716-11719, 2002.

[33] Haiming Zhu, M. Tuan Trinh, Jue Wang, Yongping Fu, Prakriti P. Joshi, Kiyoshi Miyata, Song Jin, and X.-Y. Zhu, "Organic Cations Might Not Be Essential to the Remarkable Properties of Band Edge Carriers in Lead Halide Perovskites," *Adv. Mater.,* vol. 29, p. 1603072, 2017.

[34] Rebecca L. Milot, Rebecca J. Sutton, Giles E. Eperon, Amir Abbas Haghighirad, Josue Martinez Hardigree, Laura Miranda, Henry J. Snaith, Michael B. Johnston, and Laura M. Herz, "Charge-Carrier Dynamics in 2D Hybrid Metal−Halide Perovskites," *Nano Lett.,* vol. 16, p. 7001−7007, 2016.

[35] Kiyoshi Miyata, Daniele Meggiolaro, M. Tuan Trinh, Prakriti P. Joshi, Edoardo Mosconi, Skyler C. Jones, Filippo De Angelis, X.-Y. Zhu, "Large polarons in lead halide perovskites," *Sci. Adv.,* vol. 3, no. 8, p. 1701217, 2017.

[36] Lionel Duvillaret, Frédéric Garet, and Jean-Louis Coutaz, "A Reliable Method for Extraction of Material Parameters in Terahertz Time-Domain Spectroscopy," *IEEE Journal of Selected Topics in Quantum Electronics,* vol. 2, no. 3, pp. 739-746, 1996.

[37] Jun Kang and Lin-Wang Wang, "High Defect Tolerance in Lead Halide Perovskite CsPbBr3," *J. Phys. Chem. Lett,* vol. 8, p. 489−493, 2017.